ADVANCED ELECTRONIC MATERIALS Open Access
www.advelectronicmat.de

Electrochemical Ionic Synapses with Mg^{2+} as the Working Ion

*Miranda Schwacke, Pjotrs Žguns, Jesús del Alamo, Ju Li, and Bilge Yildiz**

Dynamic doping by electrochemical ion intercalation is a promising mechanism for modulating electronic conductivity, allowing for energy-efficient, brain-inspired computing hardware. While proton-based devices have achieved success in terms of speed and efficiency, the volatility and environmental pervasiveness of hydrogen (H) might limit the robustness of devices during fabrication, as well as the long-term retention of devices after programming. This motivates the search for alternative working ions. In this work, a proof-of-concept is demonstrated for electrochemical ionic synapses (EIS) based on intercalation of Mg^{2+} ions. The reported device has a symmetric design, with Mg_xWO_3 used as both the gate and channel material. Increasing the Mg fraction, x, in WO_3 increases the electronic conductance in a continuum over a large range (80 nS — 2 mS). Ex situ characterization of the channel confirms that modulation of channel conductance is due to Mg^{2+} intercalation. Unlike H-EIS which rapidly loses programmed conductance states over a few seconds when exposed to air, Mg-EIS can be operated and has good retention in air, with no sign of degradation after 1 h. Mg^{2+} as a working ion with WO_3 as the channel is a promising material system for EIS with long-term retention and low energy consumption.

1. Introduction

The rapid rise in the energy consumed by computing compared to the world's energy production motivates the search for new computing paradigms capable of dramatically improving the energy efficiency of computing. A recent goal set by the Semiconductor Research Corporation Decadal Plan calls for 1000 000-fold improvement in the energy efficiency of computing over the next decade.[1] One area of computing where there is significant room for improvement in energy efficiency is machine learning. The von Neumann structure of traditional computer systems separates CPU and memory, a suboptimal configuration for machine learning algorithms as it requires frequent transfer of data between computation and memory for retrieving and updating states.[2] An alternative to implementing machine learning algorithms on traditional computer systems is to instead use physical neural networks in the analog domain. These physical neural networks consist of crossbar arrays with programmable resistors sitting at the crosspoints.[3] The crossbar configuration imitates the connectivity of neurons, while the programmable resistors act as artificial synapses where the analog synaptic state is stored as the electronic resistance of an active material.[4,5] Several types of resistive switching mechanisms have been widely studied, including by formation and rupture of conducting filaments (CF) and Joule heating-induced phase transformations, but these mechanisms are limited by variability/stochasticity and high energy consumption and drift, respectively.[6,7]

Recently, there has been increasing interest in a new mechanism, resistance modulation by ion insertion or dynamic doping.[8] Insertion of suitable positive ions into an appropriate semiconducting material is accompanied by electron doping, which can change the resistance of the material. Here we refer to devices operating by this mechanism as electrochemical ionic synapses (EIS),[9] and in the literature they are also referred to as electrochemical random-access memory (ECRAM).[10] EIS has been demonstrated using protons,[11–19] lithium ions,[8,20–25] oxygen ions,[26–31] and copper ions[32] as the working ion.

In order for EIS to be a practical device choice for training analog neural networks (ANNs), it must be possible to program them with pulses as short as 1 ns, and with operating voltages of 1 V or less.[3] Furthermore, they must be able to traverse 100–1000 different nonvolatile conductance states spanning at least ≈1 order of magnitude in conductance.[3] EIS must also have good

M. Schwacke, P. Žguns, J. Li, B. Yildiz
Department of Materials Science and Engineering
Massachusetts Institute of Technology
Cambridge, MA 02139, USA
E-mail: byildiz@mit.edu
J. del Alamo
Microsystems Technology Laboratories
Massachusetts Institute of Technology
Cambridge, MA 02139, USA
J. Li, B. Yildiz
Department of Nuclear Science and Engineering
Massachusetts Institute of Technology
Cambridge, MA 02139, USA

The ORCID identification number(s) for the author(s) of this article can be found under https://doi.org/10.1002/aelm.202300577

DOI: 10.1002/aelm.202300577

endurance, continuing to operate for over 10^{10} programming pulses and retaining stored conductance states for a training epoch.[9]

EIS based on proton movement has already shown great promise. Recently, Onen et al. demonstrated modulation of WO_3 by proton insertion with pulses as short as 5 ns.[13] The materials used in this work were all CMOS compatible, and devices were scaled down to 30 nm × 60 nm dimensions in active area.[13] Furthermore, devices showed reasonably linear and symmetric modulation of states and consumed only ≈15 aJ per pulse for proton transfer (≈2.7 fJ when including dynamic energy dissipation).[13] This very fast and low energy resistance modulation is enabled by the small ionic size and resulting high diffusivity of protons in many solids. However, the high diffusivity of protons also has disadvantages. Proton-based EIS are generally sensitive to the environment in which they operate. First, many proton conductors are dependent on adsorbed/absorbed water, limiting their use in dry environments.[33] Second, even for devices with proton conductors which can operate in dry environments, protons are removed from the active layer (channel) by oxidation to form water when exposed to air or oxygen-containing environments.[11] This leads to rapid loss in stored conductance states.[11] This problem can be alleviated by encapsulation of devices.[34] However, encapsulation may not immediately follow protonation in the integrated circuit fabrication process, making it difficult to retain protons within the device during fabrication. Furthermore, even when encapsulated, the active material of a device will always need to be contacted by a metal to measure its resistance. Given the high diffusivity of hydrogen in most metals, especially those with high electronic conductivity which are used as interconnects, these metal contacts could allow for hydrogen diffusion out of the active channel material and a loss of stored states.

Similarly, in O-EIS it has been observed that after being programmed to a high conductance state, the WO_{3-x} channel conductance slowly decreases over time. This is attributed to slow oxidation of the channel by oxygen in air, even when HfO_2 passivation layers are used to protect the device from the atmosphere.[35] Furthermore, O-EIS devices typically must be operated either using high voltages[26,28,31] or at elevated temperatures[29,35] to overcome the high activation energies for O^{2-} ion migration.

These challenges with H-EIS and O-EIS motivate our search into alternative ions. The larger ionic radius of Mg^{2+} compared to H^+ is expected to help improve retention, while the lack of gas volatility and insulating nature of possible Mg_xWO_3-O_2 reaction products should allow for containment of Mg^{2+} ions within devices in air even without encapsulation, making devices more robust to the fabrication process and insensitive to the environment. At the same time, Mg^{2+} migration should still have faster kinetics compared to O^{2-}. In particular, in amorphous WO_3 films the diffusion coefficient of oxygen vacancies at room temperature is reported to be on the order of 10^{-17} cm^2 s^{-1},[36] while the diffusion coefficient of Mg^{2+} ions at room temperature is reported to be 10^{-10} – 10^{-11} cm^2 s^{-1}.[37] Furthermore, Mg^{2+} solid electrolytes typically have higher ionic conductivities than O^{2-} electrolytes. At 300 °C, state-of-the-art oxygen-ion-conductors have ionic conductivities of up to ≈10^{-4} S cm^{-1}.[38] The ionic conductivities of these materials at room temperature are seldom reported, but extrapolation assuming oxygen diffusion in these materials obeys Arrhenius law yields values of ≈10^{-12} S cm^{-1}. By comparison, there have been reports of solid Mg^{2+} electrolytes with ionic conductivities in the 10^{-5} S cm^{-1} range at room temperature.[39]

Unlike Li^+, Mg^{2+} is compatible with silicon-processing and MgO is already used in magnetic random access memory technology.[40] Furthermore, Mg^{2+} is abundant, inexpensive, and has already been demonstrated in battery applications.[41,42] To our knowledge, we present here the first demonstration of EIS using Mg^{2+} as the working ion.

2. Device Configuration and Materials

The channel material used in this study is WO_3. The conductivity of WO_3 is known to increase upon insertion of many small ions, and thus it is a popular choice of channel material for EIS devices.[11,13,20,21] Furthermore, WO_3 has been shown previously to intercalate Mg^{2+} ions when used as a cathode for Mg batteries.[43,44] We also choose to use Mg_xWO_3 as the material for the ion reservoir (that is also the gate in this structure). Generally, for EIS the gate and channel materials do not need to be the same. However, this symmetric design should reduce the open-circuit potential (OCP) to near 0 V. Li et al. show that the operating voltage for Li-EIS can be reduced to 200 mV using a symmetric design with Li_xTiO_2 as both the ion reservoir and the active layer.[22] Furthermore, Mg metal, while a more obvious choice as a Mg ion reservoir, is very reactive and forms ion-blocking interfacial phases in contact with many electrolyte materials.[45,46]

For the electrolyte, we use a phase convertible electrolyte (PCE) consisting of succinonitrile mixed with an Mg salt, $Mg(TFSI)_2$. This electrolyte has been reported to have a very high Mg ion conductivity of 2.8×10^{-5} S cm^{-1}.[45] While its organic nature and low melting point (< 59 °C)[45] make it incompatible with CMOS processing, it also makes this electrolyte easy to deposit by simply dropping the melted solution on top of the channel. The combined high ionic conductivity and ease of deposition make it a good starting point for providing a proof-of-concept for Mg-EIS and allow us to focus on how Mg^{2+} interacts with the channel material.

Device fabrication is done by depositing the channel and ion reservoir layers separately on different substrates, and then sandwiching them together with the electrolyte in between during the final step, as shown in **Figure 1a**. The first step in device fabrication is sputter deposition of 5 nm thick Cr and 25 nm thick Au contacts through shadow masks on sapphire substrates to serve as source and drain. The region between source and drain (across which conductance is measured) is length (l) × width (w): 100 µm × 500 µm. Here we use l/w to designate the length/width of the region between the source and drain, while we use L/W to designate the total area of the WO_3 film. On top of the contacts, we sputter deposit a WO_3 film through a shadow mask to serve as the channel or ion reservoir. The WO_3 film used here covers $L \times W$: 1 × 0.6 cm and is 80 nm thick. After annealing at 450 °C in ambient air for 1 h to obtain the desired phase, we electrochemically insert Mg^{2+} into the ion reservoir film via a standard battery configuration with Mg metal as the ion source (anode) and the same PCE described above as the electrolyte. Once we have inserted Mg into the WO_3, we remove the Mg metal and electrolyte from the Mg_xWO_3 film. Next, we drop the melted PCE electrolyte solution on top of the channel WO_3 film and then place the substrate with the ion reservoir Mg_xWO_3 film on top such that the

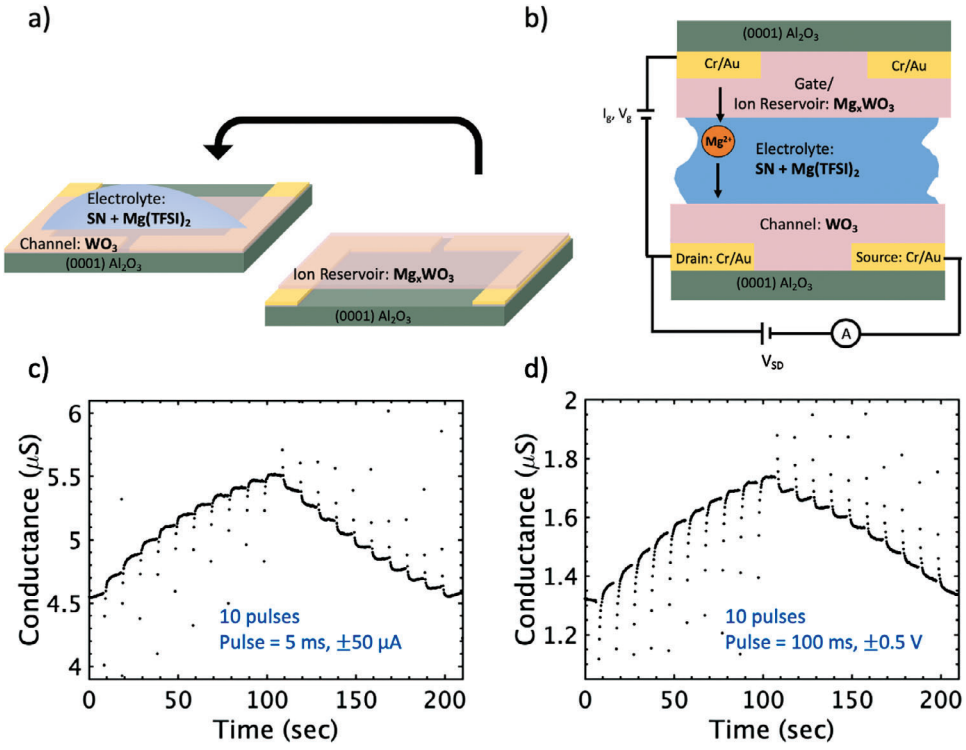

Figure 1. a) Schematic of final step in assembly of Mg-EIS devices. Fabrication of Mg-EIS devices is done by depositing the WO_3 channel and ion reservoir layers separately on different substrates. After Mg ions are inserted into the WO_3 ion reservoir electrochemically from Mg metal to form Mg_xWO_3, the ion reservoir and channel films are sandwiched together with the electrolyte in between. b) Schematic of symmetric Mg-EIS device as assembled. Channel conductance during application of c) constant current and d) constant voltage pulses.

Mg_xWO_3 film is also in contact with the electrolyte. Finally, we clamp the entire stack together to give us a complete Mg-EIS device. A schematic of the full Mg-EIS device is shown in Figure 1b.

Upon application of a positive gate voltage $+V_G$, Mg^{2+} ions migrate from the top Mg_xWO_3 layer, which acts as both the gate and ion reservoir, through the electrolyte, and into the bottom WO_3 channel, while electrons move in the same direction along the outer circuit. We measure the channel conductance by applying a small voltage (0.1 V) between the source and drain. The conductance of the channel can be decreased by the application of a negative gate voltage $-V_G$, upon which both ions and donated electrons leave the channel and return to the ion reservoir.

We have reported previously that in H-EIS, electrons donated to the channel material fill in-gap states, increasing the carrier concentration and electronic conductivity of the channel material.[9,11] We expect a similar mechanism for channel conductance modulation to occur in Mg-EIS. To confirm this, we have performed first-principles calculations of the electronic structure of Mg_xWO_3, focusing on the low concentration regime ($x = 1/64 = 1.6\%$). We observe that the inserted Mg donates two electrons to the host lattice, WO_3, resulting in formation of two small polarons (**Figure 2a**). Each polaron localizes in the (100) plane, with magnetization density centered on a single W atom and magnetization tails spreading out in-plain to four neighboring W atoms (Figure 2a). This agrees with the electron spin resonance measurements[47] and previous computational studies,[11,48] that report a similar 2D pattern of electron spread-out. The polaronic in-gap state is located ≈0.4 eV below the conduction band minima (CBM) (Figure 2b), which is close to previous first-principles calculations of polaronic levels (from ≈0.3 to 0.6 eV below the CBM).[11,48,49]

3. Device Characteristics

Both constant current and constant voltage pulses can be used for programming EIS devices. While voltage gating (Figure 1d) is preferable for the application of EIS to ANN training,[3] current gating (Figure 1c) allows us to theoretically understand exactly how many ions and electrons are transferred per pulse and directly correlate the change in channel conductance to change in ion concentration.

To investigate the achievable conductivity range and minimum programming voltage required for Mg intercalation into WO_3, we perform slow galvanostatic intercalation of Mg^{2+} into a fresh WO_3 film with a constant current of 1 nA (**Figure 3a**). The device structure used for this experiment is slightly different from the standard device structure described above in that the channel film has smaller volume ($L \times W \times t = 1.2$ mm $\times$ 0.6 mm $\times$ 15 nm). Thus, the ion reservoir ($L \times W \times t = 1$ cm $\times$ 0.6 cm $\times$ 80 nm) has 440× the volume of the channel. This was done so that the measured change in voltage is only due to changes in the channel. We calculate x in the channel by assuming that all passed charge results in Mg^{2+} ion insertion. As x in the Mg_xWO_3 channel changes between nominally 0 and 0.21, the conductivity changes from 15 mS cm^{-1} to 230 S cm^{-1} and the EIS voltage changes from −0.13 V to 0.23 V. The voltage measured here

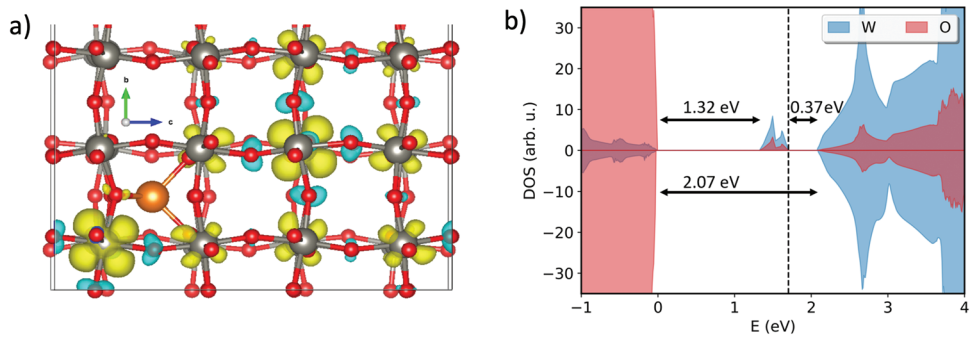

Figure 2. Mg_xWO_3, $x = 1/64$, in $P2_1/n$ monoclinic phase.[50] a) Supercell structure and magnetization density, showing localization of two polarons in the (100) plane. Color code: Mg is orange, W is grey, O is red. Magnetization density is shown with yellow (spin-up) and blue (spin-down). The first polaron has 0.68 μ_B magnetic moment on W, which is the first nearest neighbor of Mg^{2+} ($d_{Mg-W} = 3.24$ Å); the second polaron has 0.59 μ_B magnetic moment on W, which is the second nearest neighbor of Mg^{2+} ($d_{Mg-W} = 6.24$ Å). b) Density of States (DOS) projected onto W and O states. Polaronic in-gap state is seen ≈0.4 eV below the conduction band.

provides an approximation of the OCP and a lower bound on the programming voltage that will be needed for devices implemented in this material system. It is promising here that the OCPs corresponding to the upper and lower conductance states with four orders of magnitude difference are well within ± 0.25 V. For application to ANN training, only a 10× change between the highest and lowest conductance states is needed.[3] A factor of 10 change in conductance is acheivable in this device with only 110 mV change in OCP (Figure 3b).

To understand how the conductivity (σ) of Mg_xWO_3 responds to changes in x, we can examine the derivative of σ with respect to x ($d\sigma/dx$) as shown in Figure 3c. It is evident that $d\sigma/dx$ is not constant with respect to x. Therefore, for Mg-EIS devices, we can expect that the change in conductance per pulse (ΔG) will be dependent on the current Mg concentration (x) and consequently the starting conductance (G_0). This is indeed the case as shown in Figures 3d and 3e. For 500 ms, ± 10 µA pulses, when $G_0 \approx$ 4–6 µS, $\Delta G \approx 0.3$ µS pulse^{-1} (Figure 3d). When the device is in the tens of µS conductance regime, ΔG per pulse is more than three times that at ≈1 µS (Figure 3e). There is some asymmetry between potentiation and depotentiation, likely originating from electronic leakage through the electrolyte during the read periods. This electronic leakage will be discussed in more detail in Section 5. This changing ΔG per pulse with G_0 is

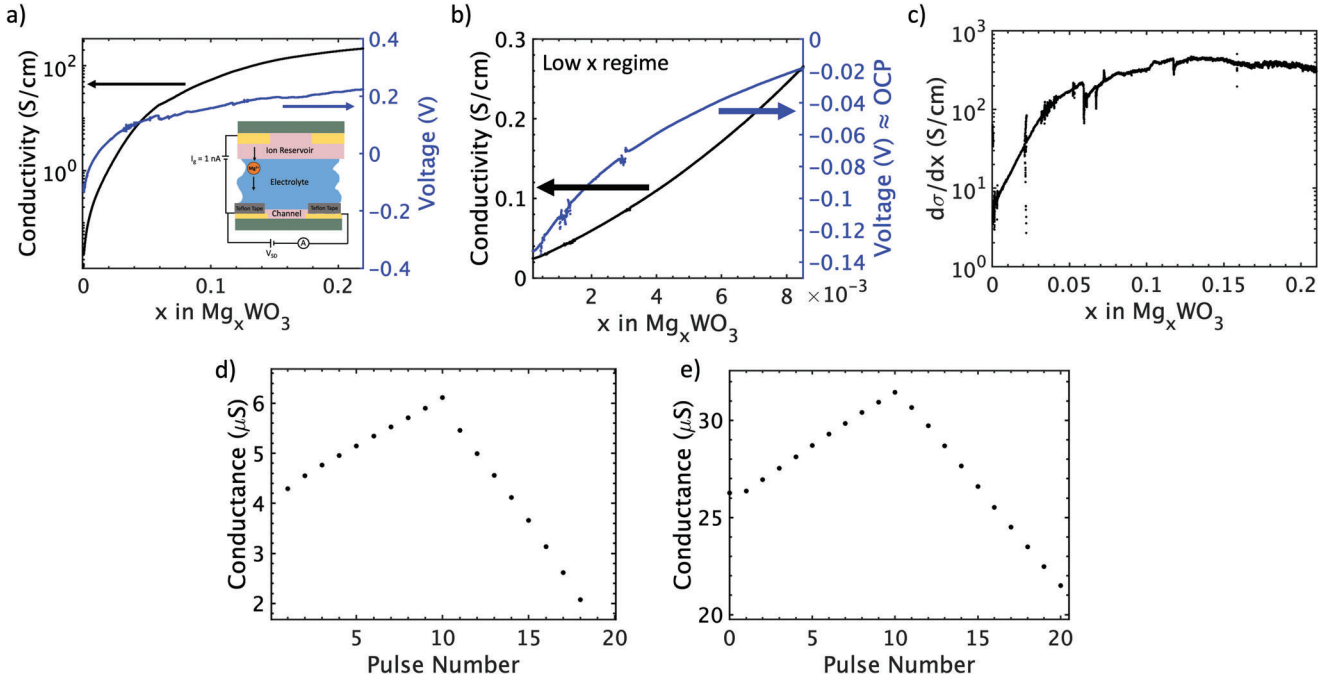

Figure 3. a,b) Channel conductivity and the EIS cell voltage during galvanostatic intercalation of Mg^{2+} into WO_3 with a current of 1 nA, showing a) four orders of magnitude change in conductivity and b) 10× change in conductivity. c) Derivative of conductivity data from (a). It is clear that $d\sigma/dx$ is not constant with respect to x. d,e) Channel conductance after potentiation and depression by application of ten ± 10 µA, 500 msec pulses when the device is d) in the 4–6 µS conductance range and e) in the 10 µS conductance range.

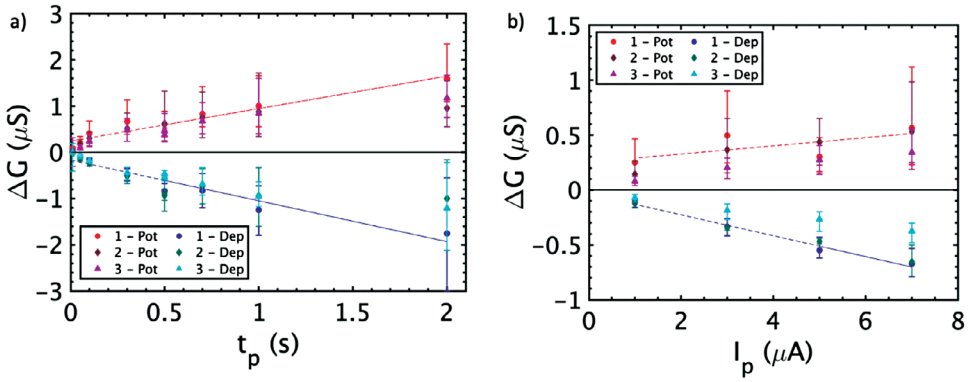

Figure 4. Dependence of change in active layer conductance (ΔG) on a) pulse duration (t_p) when the applied current is held constant (I_p = 10 μA) and b) applied current when the pulse duration is held constant (t_p = 500 msec). ΔG is linearly dependent on $\Delta Q = I_p \times t_p$. All data is taken for G_0 in the tens of μS range. The labels "1", "2", and "3" in the legend reflect data taken from three different devices (all with identical dimensions). For Device 3, data is taken after the application of over 20 000 pulses.

consistent with what has been observed for H insertion in WO_3.[11]

Besides the conductance of the channel, ΔG is also dependent on the amplitude (current or voltage) and duration of the pulse (t_p). When the change in channel conductance is small, ΔG should be linearly proportional to the charge transfer per pulse: $\Delta G \propto \Delta Q = I_p \times t_p$, as has been reported for EIS based on other working ions.[8,25,30,51] We confirm that this is also the case for Mg-EIS. For several individual devices, we apply ten potentiation pulses followed by ten depression pulses for three cycles, using a range of pulse durations and current magnitudes. **Figure 4** shows that ΔG is linearly related to both pulse duration (Figure 4a) and pulse current (Figure 4b). Furthermore, this relationship is consistent across different devices of identical dimensions and does not change even after the application of over 20 000 pulses. It should be noted that the distribution of ΔG values, visualized as error bars between the 15th and 85th percentiles in Figure 4, is not representative of random error or statistical variation in the behavior of the device. On the contrary, we expect ΔG to be dependent on G_0, and with each applied pulse G_0 changes. Therefore, the variation in ΔG reflects the variation in G_0 over ten pulses. This is especially evident when I_p or t_p (and thus ΔG) are large. This causes the variation in G_0 over ten pulses to also be quite large, which in turn causes significant variation in ΔG. Thus, instead of random error these distributions can be thought of as deviations from linearity in the channel conductance dependence on charge transferred.

While the pulse lengths and current amplitudes used here are quite large compared to most EIS devices, this is due to the large total area of the WO_3 ($W \times L$: 1 cm × 0.6 cm). The charge transferred per pulse needed for a certain $\Delta\sigma$ should scale with the total volume of the WO_3 film, assuming that the concentration of Mg is uniform throughout the channel. This is indeed the case for Mg-EIS as shown in Figure S6 (Supporting Information). Once devices have been scaled down to the target area for device applications (≈100×100 nm^2), even shorter pulses and smaller currents will be sufficient for programming the device.

Figure 5 shows the behavior of a Mg-EIS device as the channel conductance is potentiated and depressed across 100 conductance states in each cycle for 200 cycles (100 positive, 100 negative), using pulses of ±1 V, 500 msec. The conductance of the channel is read after every 5 pulses. Over many cycles there is little change in the magnitude of conductance change per pulse, consistent with the data shown in Figure 4. The slight increase in conductance over the course of the measurement originates from the voltage-controlled pulse scheme. For these devices, the open-circuit potential (OCP) is likely on the same order of magnitude as the programming voltages. Under voltage-gating, this makes the change in conductance per pulse sensitive not only to the applied voltage, but also to the initial OCP. Therefore, if each cycle begins from an OCP < 0 V, then there is a pre-existing driving force for Mg insertion into the channel, and we might expect the cycle to end at a higher conductance even if the same number of positive and negative voltage pulses are applied (Note S2, Supporting Information). This is consistent with what is observed in Figure 5.

While the data in Figure 5 shows consistent potentiation/depression behavior of a Mg-EIS device over many programming events, it lacks symmetry and linearity. Our previous work has shown that the choice of conductance regime for H-EIS device operation can significantly impact the observed linearity and symmetry of the device under current gating, due to changes in the slope of conductivity versus x in H_xWO_3.[11] Data in Figures 3a,b also suggests that both the sensitivity of Mg_xWO_3 conductivity and the slope of the OCP against inserted charge varies significantly across the large range in x probed. Thus, the linearity of Mg-EIS devices under voltage gating may be improved by careful choice of the conductance range during operation, such that $d\sigma/dx$ is large and dV_{OCP}/dx is small.

4. Confirmation of Mg^{2+} Intercalation into WO_3

To confirm that the observed changes in channel conductance under the application of current and voltage pulses are due to the intercalation of Mg ions into WO_3, we have potentiated several devices each to a high conductance level, and then disassembled these devices and performed Energy-Dispersive X-ray Spectroscopy (EDS), X-ray Diffraction (XRD), and X-ray Photoelectron Spectroscopy (XPS) ex situ on each of the WO_3 layers serving as the channel.

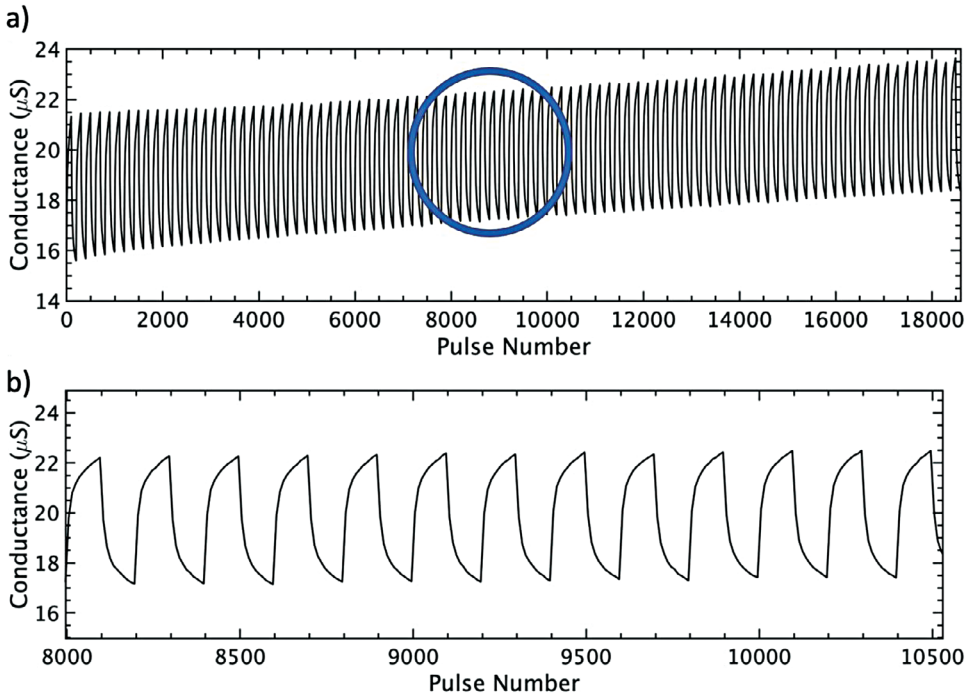

Figure 5. a) Active layer conductance after one-hundred +1 V, 500 msec pulses followed by one-hundred -1 V, 500 msec pulses. There is a delay time of 1s between pulses, except for after every 5 pulses when the conductance is read for 10 sec. This is repeated for one-hundred cycles. b) Magnified view of data within the circle in (a).

Since the penetration depth of EDS is on the order of microns, the WO_3 films used for this analysis were deposited to be 1 μm thick. Only a weak Al signal from the Al_2O_3 substrate was detected, suggesting that most of the signal originated from the WO_3 film. The existence of a clear Mg signal in EDS spectra confirms that Mg has been inserted into WO_3. However, the concentration of Mg is not uniform laterally across the channel. The calculated Mg concentration from the EDS spectra varies from below the detection limit for EDS ($x \approx 0.05$) to $x = 0.33$ across the sample (**Figure 6a**). There is no clear pattern to this non-uniformity in Mg concentration. It is possible this is due to non-uniform interfacial contact between the electrolyte and channel. The nominal Mg concentration in this film was $x = 0.25$, assuming that all charges inserted into the channel during potentiation resulted in Mg^{2+} ion insertion.

Grazing Incidence X-ray Diffraction (GIXRD) of 80 nm thick WO_3 films after annealing indicates that they are polycrystalline with a monoclinic phase (Figure 6b). For thicker films (1 μm) the (020) peak at 23.7° which is characteristic of the monoclinic phase is clearly present. While this peak cannot be seen in thinner films (80 nm) used for most devices, the (002) and (200) peak positions at 23.2° and 24.4°, respectively, are still consistent with monoclinic WO_3. For Mg_xWO_3 films which have been potentiated to nominally $x = 0.3$, there is the beginning of a phase transformation from monoclinic to tetragonal, with peaks from both phases contributing to the XRD pattern. The monoclinic to tetragonal phase transition has been observed previously for Mg_xWO_3[44] as well after the insertion of H^+ ($x > 0.1$) and Li^+ ($x > 0.015$) ions into WO_3.[11,52]

XPS was used to investigate the chemical changes in the channel during Mg^{2+} insertion. Binding energies were calibrated by charge correcting the C 1s peak to 285.0 eV. Survey data (Figure S2, Supporting Information) of a WO_3 film used as channel prior to device fabrication detects only W, O, and C. For a Mg_xWO_3 film which had been potentiated to nominally $x = 0.3$, a Mg KLL peak is clearly seen at 306 eV, confirming the presence of Mg and that Mg retains its oxidation state of Mg^{2+} upon insertion into WO_3.[53] Furthermore, no other elements are detected, suggesting that no interfacial phases form between the channel and electrolyte during potentiation. The oxidation state of W was probed by the W 4f peaks (Figure 6c,d). For the as-annealed WO_3, the W $4f^{7/2}$ and W $4f^{5/2}$ peaks are located at 35.9 eV and 38.0 eV, respectively. This is consistent with W^{6+}.[54,55] After potentiation, the positions of these peaks shift slightly to 35.6 eV and 37.6 eV. This could be due to the structural phase transition of WO_3 from monoclinic to tetragonal.[56] Additionally, there are new W 4f peaks, suggesting multiple chemical states of W are present. The new W $4f^{7/2}$ peaks are located at 34.3 eV and 33.0 eV, consistent with W^{5+} and W^{4+}, respectively.[54,55] Given that XRD suggests multiple crystal phases are present in the $Mg_{0.3}WO_3$ films, it is possible that this last peak at 33.0 eV could also be attributed to W^{5+} in a different crystal structure. However, its location is more consistent with literature values for W^{4+} (33.1 eV) than W^{5+} (34.1 eV).[54,55] Fitting of the W 4f peaks suggests the ratio of W^{6+}:W^{5+}:W^{4+} to be 1:0.5:0.06, corresponding to $Mg_{0.25}WO_3$. While at this time we cannot be sure how evenly distributed Mg^{2+} ions are within the channel, the reasonable agreement in Mg concentration found by EDS (which has a penetration depth ≈1 μm) and XPS (penetration depth ≈10 nm) suggests that at

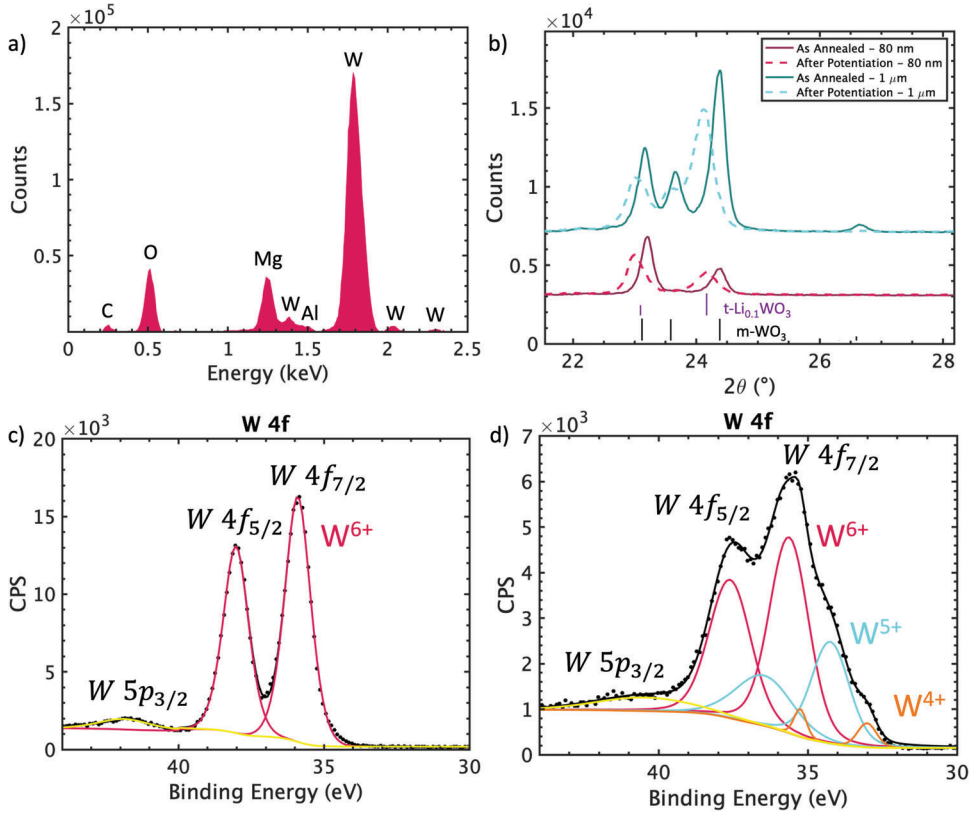

Figure 6. Ex situ chemical analysis of potentiated Mg_xWO_3 channel. a) EDS spectra of potentiated channel which is 1 μm thick. The clear Mg peak indicates Mg has been inserted into the film. Based on ZAF analysis, the Mg content at this location is $Mg_{0.33}WO_3$. b) GIXRD of as annealed (solid lines) and potentiated (dashed lines) WO_3 channel films. Red data is collected from a film which is 80 nm thick (typical thickness for Mg-EIS devices). Blue data is collected from a film which is 1 μm thick. Monoclinic WO_3 reference pattern is from PDF #00-043-1035.[57] Tetragonal $Li_{0.1}WO_3$ reference pattern is from PDF #04-015-6962.[58] c,d) W 4f emission peak of 80 nm thick WO_3 channel films, measured by XPS, (c) in the as-annealed state and (d) after potentiation to nominally $Mg_{0.3}WO_3$. The oxidation state of W is determined from the W $4f^{7/2}$ peak position. Annealing conditions are the same for all devices and films used for ex situ characterization (450 °C for 1 h in ambient air).

the time scales used for ex situ characterization (5 days) Mg is distributed through the thickness of the channel and is not just concentrated near the channel/electrolyte interface.

5. Comparisons with H-EIS

We base our comparisons of Mg-EIS to H-EIS based on the H-EIS device reported in our earlier work by Yao et al.,[11] which also used WO_3 as the active material, sputtered and annealed by the same recipe used in this work. The conductivity of WO_3 changes as a function of both Mg^{2+} and H^+ ion concentration. As shown in **Figure 7a**, it is possible to operate the devices in a conductance regime where the response looks very similar for pulses resulting in the same change in electron concentration in each device. Figure 7b shows the conductivity of WO_3 as a function of the number of inserted electrons per WO_3 formula unit ($y = 2x$ for Mg^{2+} in Mg_xWO_3, $y = x$ for H^+ in H_xWO_3). Here ions are inserted by current pulses (as opposed to constant current as in Figure 3a). For the Mg-EIS device the pulses used are 10 μA and 0.5 s long with a 10-s delay between pulses. For the smaller H-EIS device the pulses are 0.5 μA and 5 ms long with 1s between pulses. These pulsing conditions were chosen such that, given the differing dimensions of the two devices, the change in the concentration of donated electrons in the channel is the same for each device; each pulse corresponds to $\Delta y \approx 1 \times 10^{-4}$. Note that for the H-EIS device, the starting conductivity (before any programming pulses are applied) is 1.9×10^{-6} S cm^{-1}, while for the Mg-EIS device the starting conductivity is 5.5×10^{-3} S cm^{-1}. The WO_3 films for both devices are deposited and annealed using the same recipe, and XPS suggests that prior to device assembly the only W oxidation state present is W^{6+} in both cases. Therefore, this discrepancy in the magnitude of the starting conductivity may be due to electronic leakage in the Mg-EIS device (discussed later in Section 5) prior to the measurement. The conductivity of the H-EIS device reaches the starting conductivity of the Mg-EIS device at $y = 0.03$, giving us an idea of the uncertainty on y in Mg-EIS for our measurement. It is also possible that other slight variations in the deposition and annealing conditions (e.g., ambient humidity, time between annealing and device assembly) could cause differences in the WO_3 films which are not captured by XPS but affect the conductivity.

In the lower electron concentration regime ($y < 0.36$), the conductivity of $Mg_{y/2}WO_3$ increases much faster than H_yWO_3 with increasing y, resulting in $Mg_{y/2}WO_3$ having higher conductivity than H_yWO_3 for the same y. This is also evident in the change in

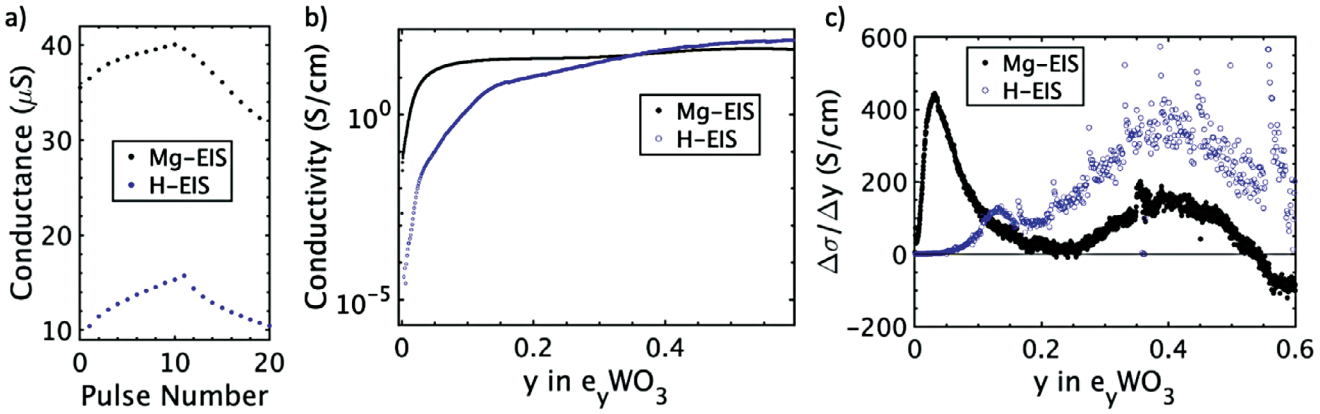

Figure 7. a) Conductance states of Mg-EIS and H-EIS device as ten positive and ten negative current pulses are applied in low electron concentration regimes ($y \approx 0.01$ for Mg-EIS and $y \approx 0.1$ for H-EIS). For the Mg-EIS device the pulses used are 10 μA and 0.5 s long with a 10-s delay between pulses. For the smaller H-EIS device the pulses are 0.5 μA and 5 ms long with 1s between pulses. For both devices, each pulse corresponds to $\Delta y \approx 1 \times 10^{-4}$ b) Conductivity of Mg-EIS and H-EIS device as a function of the number of electrons inserted per WO_3 formula unit. c) Change in conductivity ($\Delta\sigma/\Delta y$) in response to a pulse for which $\Delta y = 1.95 \times 10^{-4}$.

conductivity ($\Delta\sigma/\Delta y$) shown in Figure 7c (essentially a derivative of the data in Figure 7b). For the Mg-EIS device there is a large peak at $y \approx 0.03$, while for the H-EIS device $\Delta\sigma/\Delta y$ is three orders of magnitude smaller than the Mg-EIS device at $y \approx 0.03$. However, at higher electron concentrations ($y > 0.15$), the conductivity of H_yWO_3 increases at a similar rate to $Mg_{y/2}WO_3$. These results indicate that while the larger size of Mg^{2+} compared to H^+ may create more stress in the lattice for the same number of inserted ions, fewer Mg^{2+} ions may be needed compared to H^+ to achieve the same change in conductivity in the low ion concentration regime.

The reason for the increased sensitivity (Figure 7c) of Mg-EIS compared to H-EIS is intriguing. We have compared the electronic structures of Mg_xWO_3 and $H_{2x}WO_3$, keeping the donated electron concentration the same for the two cases. The filling of polaronic in-gap states upon H and Mg insertion in WO_3 is a similar characteristic in the electronic structure, but there are two key differences between Mg_xWO_3 and $H_{2x}WO_3$, both of which can contribute to an increased sensitivity of electronic conductivity in Mg_xWO_3 compared to $H_{2x}WO_3$. First, in Mg_xWO_3, the defect level appears higher in the gap closer to the CBM, at ≈0.4 eV below the CBM, versus 0.8 eV below CBM in $H_{2x}WO_3$. This indicates that the Fermi level and the electronic carrier concentration is higher in the case of Mg_xWO_3 compared to $H_{2x}WO_3$. Second, in Mg_xWO_3 polarons are more spread-out (the central W magnetic moments are smaller by ≈15% than in $H_{2x}WO_3$), suggesting that polaron trapping by Mg^{2+} is weaker than that by H^+ (see Figure 2; Figure S9, Supporting Information). In Mg_xWO_3 one of the polarons is localized on the W that is the next nearest neighbor to Mg^{2+}, which also contributes to a weaker localization as seen by its magnetic moment (see Figure 2a caption). This weaker trapping of polarons could decrease the polaron migration barrier and increase the polaron mobility in Mg_xWO_3 as compared to $H_{2x}WO_3$. Both of these differences could contribute to the increased sensitivity of the electronic conductivity of WO_3 to Mg insertion versus the H insertion in the EIS.

Another possible explanation is that due to the larger size of Mg^{2+} compared to H^+, Mg^{2+} has lower diffusivity than H^+ in WO_3 and thus takes longer to be distributed evenly across the channel. Concentration of Mg^{2+} in certain regions of the channel (e.g., along grain boundaries or near the electrolyte/channel interface at short time scales) could explain an increased rate of conductance change. This mechanism is yet to be quantitatively shown in this system.

We have estimated the energy consumption of our devices using the gate current and gate voltage during the pulse (not including dynamic energy dissipation) and compared it with earlier devices. The energy consumption of our Mg-EIS devices is estimated at 90 aJ μm^{-2} nS^{-1}. As expected, given the larger size and double charge of Mg^{2+} compared to H^+, this is higher than H-EIS (18 aJ μm^{-2} nS^{-1}) but comparable order of magnitude.[11] However, Mg-EIS devices consume much lower energy than the reported energy consumption of O-EIS devices which operate without heating (2 pJ μm^{-2} nS^{-1}) after correcting for differences in l and w (Note S1, Supporting Information).[51]

The primary motivation for using Mg as the working ion as opposed to protons is the promise of improved retention of programmed conductance states, even in air. There are many reasons the channel conductance may change over time even in the absence of programming pulses: loss of working ions from the channel,[11] oxidation/reduction of the active material,[34] a leaky electrolyte, or ion redistribution within the channel.[9] While some of these conductance state loss mechanisms are reversible (i.e., a conductance state lost by leakage through the electrolyte can be re-established by the application of more programming pulses), others limit the future operation of the device. If working ions from the active layer are lost from the system, not only does the conductance of the active layer decrease, but the ion reservoir ceases to be an effectively infinite source of working ions and then the full range of conductance values can no longer be achieved. In H-EIS, the primary retention loss mechanism is often the loss of protons.

To investigate conductance state loss mechanisms in Mg-EIS, we examine the retention of the channel conductance for two different off-states: open circuit and held at 0 V constant resting potential (V_{rest} = 0 V). Open circuit condition prevents

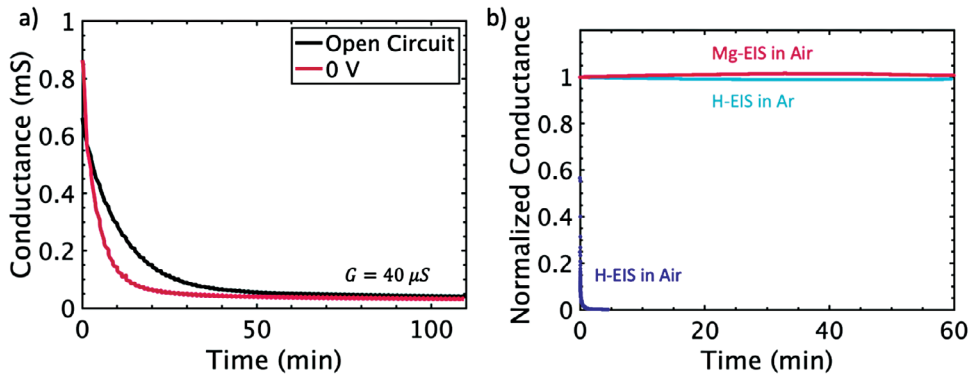

Figure 8. a) Evolution of conductance of Mg-EIS device under both open-circuit and V_{rest} = 0 V off-state conditions after being potentiated to a high conductance level. b) Normalized conductance (G/G_0) of Mg-EIS at G_0 corresponding to OCP = 0 V compared to H-EIS devices operated in air and Ar atmospheres, from.[11]

electrons from traveling along the outer circuit. Therefore, if the electrolyte is also a perfect block to electrons, then maintaining charge neutrality in the ion reservoir and channel requires that no ions move between them. If there is no mechanism for ions to leave the device (e.g., by oxidation or out-diffusion), then the conductance state should remain constant indefinitely. In contrast, if a constant resting potential is applied, then electrons and ions are free to move along the outer circuit and across the electrolyte, respectively, and will do so until the OCP of the device is equal to the applied resting potential (V_{rest} = OCP). The active layer conductance will change throughout this process, but once V_{rest} = OCP the conductance should remain constant.

Figure 8a shows the evolution of conductance of an Mg-EIS device after being potentiated to a high conductance level for both off-state conditions (open circuit and V_{rest} = 0 V). For both cases the active layer conductance decreases over time, from nearly 1 mS to ≈40 µS. For the V_{rest} = 0 V we expect this decrease in conductance until OCP = V_{rest} = 0 V. The fact that the conductance under open circuit conditions eventually settles at the same conductance value, indicates that the loss in conductance state under open circuit is also driven by the OCP. This behavior is consistent with a leaky electrolyte which allows for both electronic and ionic transport, even under open circuit conditions, albeit more slowly than if the device is held at V_{rest} = 0 V. Chronoamperometry experiments suggest that the electrolyte used in Mg-EIS devices has an electronic conductivity of ≈1×10^{-6} S cm^{-1}, ≈4% of the ionic conductivity (Figures S3 and S4, Supporting Information).

As mentioned earlier, a leaky electrolyte could also explain the discrepancy between the starting conductivity of Mg-EIS and H-EIS devices and the observed asymmetry in Figure 3c,d. Electronic leakage through the electrolyte allows for ions to also move slowly between the ion reservoir and channel layers in order to reduce the OCP of the device, even when the device is open-circuited. This means that as soon as the Mg-based device is assembled, ions may move from the ion reservoir (where they are in high concentration) to the channel (which is initially devoid of Mg ions). Since there is some finite delay time between device assembly and initial channel conductance measurements, there will be some small concentration of Mg in the channel even during the initial conductivity measurement, which can have a significant impact on the initial conductivity as WO_3 is very sensitive to doping in this low dopant concentration regime. Similarly, during the read period of any measurement, ions will slowly move across the electrolyte in the direction that minimizes the OCP. If the device is being operated in a regime where the OCP > 0 V, during the read periods the channel will lose ions, causing the final conductance state to be lower that the starting conductance state, even if equal numbers of potentiation and depression pulses are applied. We would like to note again that, while this electrolyte allowed us to start a proof-of-principle Mg-EIS and focus our study on the channel behavior, the leakiness of the electrolyte in this work is not a universal challenge for the Mg-EIS. Other inorganic and electronically insulating electrolyte alternatives can be pursued as a follow up to this work.

Figure 8b shows the channel conductance of the Mg-EIS device after it has been held at V_{rest} = 0 V for several hours and reached the conductance state corresponding to OCP = 0 V. In this state, the conductance value is very stable compared to H-EIS in air and shows similar retention to H-EIS operated in an inert atmosphere. Additional data showing retention of a Mg-EIS device at a very high conductance state over a period of three days is shown in Figure S8 (Supporting Information). This again suggests that the limits on retention of Mg-EIS in this work are due to a leaky electrolyte and possibly Mg^{2+} ion redistribution in the channel, but not loss of the working-ion as is the case of H-EIS in air. Given that the focus of this work is on WO_3 as a channel material paired with Mg^{2+} as the working ion, and we do not intend to translate the current electrolyte to real applications, this result is very promising. Future work on devices with CMOS-compatible and electronically insulating electrolytes which are practical for device applications should more carefully study the effect of device OCP and electrolyte electronic leakage on retention characteristics.

To investigate the source of the improved retention in air of Mg-EIS compared to H-EIS channels, we use density functional theory to calculate the enthalpy for the reaction of Mg_xWO_3 with

O_2 to form MgO. The reactions and the calculated reaction enthalpies are as follows:

$$Mg + 1/2\,O_2 \rightarrow MgO \quad \Delta E = -6.16\ eV \tag{1}$$

$$64\left(Mg_{1/64}WO_3\right) + 1/2O_2 \rightarrow MgO + 64WO_3 \quad \Delta E = -2.56\ eV \tag{2}$$

The reaction enthalpy is negative and therefore the reaction is thermodynamically favorable, and thus, Mg_xWO_3 is not expected to be thermodynamically stable under the standard oxygen partial pressure $PO_2 = 0.21$ atm. We propose two alternative explanations for the experimentally observed stability, both based on kinetic factors. First, the reaction of Mg_xWO_3 with O_2 may be kinetically hindered, as the conductivity of O^{2-} anions into WO_3 to react with Mg^{2+}, or of Mg^{2+} out of WO_3 to react with O_2 and precipitate as MgO at room temperature is much lower than the room-temperature proton conductivity. Second, a very thin layer of MgO may form on the edges of the Mg_xWO_3 film where it is in contact with air (as opposed to the electrolyte). Since MgO is both electronically and ionically insulating, this would be a self-limiting process; after the formation of a continuous MgO layer, further oxidation of the channel would be blocked.

6. Summary and Conclusions

Here we have provided a proof-of-concept for electrochemical ionic synapses with Mg^{2+} as the working ion. Intercalation of Mg^{2+} ions into WO_3 as a channel material allows for tuning of channel conductance over a large range (in this work, 80 nS – 2.3 mS). EDS, XPS, and XRD results confirm that this change in conductance can be attributed to Mg^{2+} insertion and the accompanying n-type electron doping of WO_3. Furthermore, compared to the intercalation of H^+ into WO_3, the intercalation of Mg^{2+} causes a greater conductance increase in the low ion concentration regime, potentially allowing one to work with smaller concentration of ions in the channel. The greatest advantage of Mg-EIS compared to H-EIS is the ability to operate devices in air without encapsulation. Unlike H^+, there is no indication from the data collected for current Mg-EIS devices that Mg^{2+} ions are lost to oxidation in air or from diffusion into metallic contacts. Current problems with retention are instead attributed to electronic leakage through the electrolyte used in this work. Furthermore, the energy consumption for Mg-EIS is comparable to H-EIS and lower than O-EIS devices. We expect that once Mg-EIS devices are scaled down to sub-micron dimensions and operated under reasonable conditions for implementation in analog neural networks, the energy consumption for ion movement should be on the order of attojoules. Future work will focus on (1) studying Mg^{2+} ion diffusion and distribution in the channel and (2) replacing the current PCE with a CMOS-compatible, scalable electrolyte with higher electronic resistance. Not only should an alternative electrolyte with higher electronic resistance allow for devices with excellent retention under open-circuit conditions and for a large range of resistance states, thin film deposition methods should produce more conformal channel/electrolyte interfaces, avoiding the observed non-uniformities in channel Mg^{2+} ion concentration arising from nonuniform electrolyte/channel contact. Nevertheless, we have shown that the Mg^{2+}/WO_3 working ion/channel material system is promising for furthering Mg-EIS as a technology for energy-efficient, brain-inspired computing.

7. Experimental Section

Materials Deposition: The Au contacts for the source, drain, and gate as well as the WO_3 films used for both gate and channel layers were deposited by RF sputter deposition on Al_2O_3 (0001) substrates. Prior to deposition, the substrates were cleaned by subsequent sonication in acetone, IPA, and DI water for 5 min each. A deposition pressure of 3 mTorr was used for all sputtered materials. First, a 5 nm Cr adhesion layer was deposited with an RF power of 120 W. Next, 25 nm thick Au contacts were deposited on top of the Cr with an RF power of 60 W. Finally, an 80 nm thick WO_3 layer was deposited from a metallic W target by reactive sputtering at an RF power of 100 W. The area of the deposited WO_3 films was 1 cm × 0.6 cm. The Ar/O_2 gas flow ratio during this process was 9.3/2.7. Post-deposition, the films were annealed at 450 °C in air for 1 h.

The PCE was prepared by mixing 1mol% $Mg(TFSI)_2$ with succinonitrile at 65 °C. The electrolyte was dropped directly onto the WO_3 film at this temperature, and then allowed to cool until it is solidified before device assembly is completed.

Device Testing: Devices were tested by application of constant current or constant voltage pulsing with 10 s between pulses using a Keithley 2400 or B1500a Semiconductor Device Analyzer. Unless otherwise specified, the conductance of the channel was read continuously throughout tests by the application of +0.1 V between source and drain ($w \times l$ = 500 µm × 100 µm). When conductance was reported as a singular value for each pulse, this is the average conductance value during the last 5 s of the read time, after the conductance value has settled. For the energy consumption calculation, constant current pulses were applied, with the resulting gate voltage being read every 2 msec.

Materials Characterization: EDS was performed inside of a JEOL 6610LV Scanning Electron Microscope equipped with an IXRF EDS system. An accelerating voltage of 20 kV was used. Elemental ratios were calculated from EDS spectra using the Iridium Ultra software. GIXRD was performed on a Rigaku Smartlab diffractometer (Cu K$\alpha\lambda$ = 1.5406 Å). XPS was done with a PHI Versaprobe II spectrometer with Al Kα source. Mg_xWO_3 films from devices were rinsed with DI water several times prior to all ex situ characterization to remove any remaining electrolyte from the surface. XPS spectra were analyzed using CasaXPS.[59]

First Principles Calculations: Density Functional Theory Calculations were performed within the Projector Augment Wave method[60] as implemented in the VASP code.[61–65] The SCAN meta-Generalized Gradient Approximation functional was employed,[66] and spin polarization was turned on. Rotationally invariant Hubbard U correction[67] was applied to W 5d states. The U value was first set to 9 eV to facilitate polaron formation and then was iteratively reduced to 5 eV for production calculations. This U value provided reasonable agreement on the polaron level positions as compared with the previous theoretical studies[11,48,49] and experimental reports of polaron shape.[47] However, we emphasize that the absolute position of the defect level is sensitive to the choice of the exchange-correlation functional (and U), and the comparison between Mg_xWO_3 and $H_{2x}WO_3$ was focused on. Plane-wave kinetic energy cut-off of 500 eV was used. The 2×2×2 large WO_3 supercell (256 atoms) was used for all calculations of Mg_xWO_3, $H_{2x}WO_3$, and WO_3 (x = 1/64). For WO_3 calculations, the monoclinic $P2_1/n$ phase[50] was used as a starting structure (the relaxed WO_3 unit cell lattice parameters were a = 7.49 Å, b = 7.48 Å, c = 7.56 Å, β = 91.0°, which is within 2.6% of the experimental values: 7.30 Å, 7.54 Å, 7.69 Å, 90.9°; due to Mg_x doping, the lattice parameters and angles of WO_3 changed as follows: Δa = 0.1%, Δb = 0.1%, Δc = −0.6%, $\Delta\beta$ = −0.5%; due to H_{2x} doping, the lattice parameters and angles of WO_3 changed as follows: Δa = −0.1%, Δb = 0.3, Δc = −0.1%, $\Delta\beta$ = 0.1%). Brillouin zone integration was performed on the Γ-centered 2 × 2 × 2 k-points mesh. Unit cell calculations were performed for rock-salt MgO, hcp Mg,

and O_2 molecule, and total energies were converged with respect to the *k*-points density (<0.02 meV per atom). Atomic coordinates were relaxed until forces fell below 10 meV $Å^{-1}$. The oxygen partial pressure correction was added to oxygen chemical potential as $k_B T \ln(p_{O2}/P_0)$, where $P_0 = 1$ atm.[68] Thus obtained reaction energies at $T = 298.15$ K and $p_{O2} = 0.21$ atm were as follows: *i*) $Mg + ½ O_2 \rightarrow MgO$, $\Delta E = -6.14$ eV $= -592$ kJ/mol; *ii*) $Mg(WO_3)_{64} + ½ O_2 \rightarrow MgO + (WO_3)_{64}$ (i.e., $x_{Mg} = 1/64 \approx 1.6\%$), $\Delta E = -2.57$ eV $= -248$ kJ mol^{-1}.

Supporting Information

Supporting Information is available from the Wiley Online Library or from the author.

Acknowledgements

This work was supported by Semiconductor Research Corporation (SRC) project #3010.001, the MIT Quest for Intelligence Program, and the Samsung Semiconductor Fellowship. This work was carried out in part through the use of MIT Materials Research Laboratory and MIT.nano's shared facilities. The authors acknowledge the Texas Advanced Computing Center (TACC) at the University of Texas at Austin for providing Stampede2 and Frontera resources that have contributed to the first-principles calculations reported within this paper. The authors thank Dr. Mantao Huang for discussion on the approach to investigate device retention.

Conflict of Interest

The authors declare no conflict of interest.

Data Availability Statement

The data that support the findings of this study are available from the corresponding author upon reasonable request.

Keywords

artificial synapses, ECRAM, EIS, Mg intercalation

Received: August 28, 2023
Revised: November 2, 2023
Published online:

[1] "Decadal Plan for Semiconductors – SRC", can be found under, https://www.src.org/about/decadal-plan/.
[2] D. V. Christensen, R. Dittmann, B. Linares-Barranco, A. Sebastian, M. Le Gallo, A. Redaelli, S. Slesazeck, T. Mikolajick, S. Spiga, S. Menzel, I. Valov, G. Milano, C. Ricciardi, S.-J. Liang, F. Miao, M. Lanza, T. J. Quill, S. T. Keene, A. Salleo, J. Grollier, D. Markovic, A. Mizrahi, P. Yao, J. J. Yang, G. Indiveri, J. P. Strachan, S. Datta, E. Vianello, A. Valentian, J. Feldmann, et al., *Neuromorph. Comput. Eng.* **2022**, *2*, 022501.
[3] T. Gokmen, Y. Vlasov, *Front. Neurosci.* **2016**, *10*, 00333.
[4] J. Shi, S. D. Ha, Y. Zhou, F. Schoofs, S. Ramanathan, *Nat. Commun.* **2013**, *4*, 2676.
[5] P. M. Sheridan, F. Cai, C. Du, W. Ma, Z. Zhang, W. D. Lu, *Nat. Nanotechnol.* **2017**, *12*, 784.
[6] H.-S. P. Wong, S. Raoux, S. Kim, J. Liang, J. P. Reifenberg, B. Rajendran, M. Asheghi, K. E. Goodson, *Proceedings of the IEEE* **2010**, *98*, 2201.
[7] J. Tang, F. Yuan, X. Shen, Z. Wang, M. Rao, Y. He, Y. Sun, X. Li, W. Zhang, Y. Li, B. Gao, H. Qian, G. Bi, S. Song, J. J. Yang, H. Wu, *Adv. Mater.* **2019**, *31*, 1902761.
[8] E. J. Fuller, F. E. Gabaly, F. Léonard, S. Agarwal, S. J. Plimpton, R. B. Jacobs-Gedrim, C. D. James, M. J. Marinella, A. A. Talin, *Adv. Mater.* **2017**, *29*, 1604310.
[9] M. Huang, M. Schwacke, M. Onen, J. Del Alamo, J. Li, B. Yildiz, *Adv. Mater.* **2022**, *35*, 2205169.
[10] A. A. Talin, Y. Li, D. A. Robinson, E. J. Fuller, S. Kumar, *Adv. Mater.* **2022**, *n/a*, 2204771.
[11] X. Yao, K. Klyukin, W. Lu, M. Onen, S. Ryu, D. Kim, N. Emond, I. Waluyo, A. Hunt, J. A. Del Alamo, J. Li, B. Yildiz, *Nat. Commun.* **2020**, *11*, 3134.
[12] M. Onen, N. Emond, J. Li, B. Yildiz, J. A. Del Alamo, *Nano Lett.* **2021**, *21*, 6111.
[13] M. Onen, N. Emond, B. Wang, D. Zhang, F. M. Ross, J. Li, B. Yildiz, J. A. Del Alamo, *Sci* **2022**, *377*, 539.
[14] E. J. Fuller, S. T. Keene, A. Melianas, Z. Wang, S. Agarwal, Y. Li, Y. Tuchman, C. D. James, M. J. Marinella, J. J. Yang, A. Salleo, A. A. Talin, *Sci* **2019**, *364*, 570.
[15] A. Melianas, T. J. Quill, G. Lecroy, Y. Tuchman, H. V. Loo, S. T. Keene, A. Giovannitti, H. R. Lee, I. P. Maria, I. Mcculloch, A. Salleo, *Sci. Adv.* **2020**, *6*, 2958.
[16] Y. Tuchman, T. J. Quill, G. Lecroy, A. Salleo, *Adv. Electron. Mater.* **2021**, *8*, 2100426.
[17] Y. Van De Burgt, E. Lubberman, E. J. Fuller, S. T. Keene, G. C. Faria, S. Agarwal, M. J. Marinella, A. Alec Talin, A. Salleo, *Nat. Mater* **2017**, *16*, 414.
[18] R. D. Nikam, J. Lee, W. Choi, W. Banerjee, M. Kwak, M. Yadav, H. Hwang, *Small* **2021**, *17*, 2103543.
[19] A. Melianas, M.-A. Kang, A. Vahidmohammadi, T. J. Quill, W. Tian, Y. Gogotsi, A. Salleo, M. M. Hamedi, *Adv. Funct. Mater.* **2021**, *32*, 2109970.
[20] D. M. Bishop, P. Solomon, S. Kim, J. Tang, J. Tersoff, T. Todorov, M. Copel, J. Collins, K. T. Lee, S. Shin, W. Haensch, J. Rozen, in *Extended Abstracts of the 2018 International Conference on Solid State Devices and Materials*, The Japan Society Of Applied Physics, Hongo Campus, The University of Tokyo, Tokyo, Japan **2018**.
[21] J. Lee, R. D. Nikam, S. Lim, M. Kwak, H. Hwang, *Nanotechnology* **2020**, *31*, 235203.
[22] Y. Li, E. J. Fuller, S. Asapu, S. Agarwal, T. Kurita, J. J. Yang, A. A. Talin, *ACS Appl. Mater. Interfaces* **2019**, *11*, 38982.
[23] R. D. Nikam, M. Kwak, J. Lee, K. G. Rajput, W. Banerjee, H. Hwang, *Sci. Rep.* **2019**, *9*, 18883.
[24] R. D. Nikam, M. Kwak, J. Lee, K. G. Rajput, H. Hwang, *Adv. Electron. Mater.* **2020**, *6*, 1901100.
[25] J. Tang, D. Bishop, S. Kim, M. Copel, T. Gokmen, T. Todorov, S. Shin, K. Lee, P. Solomon, K. Chan, W. Haensch, J. Rozen, in 2018 IEEE International Electron Devices Meeting (IEDM) **2018**, p. 13.1.1–13.1.4.
[26] Y. Jeong, H. Lee, D. G. Ryu, S. H. Cho, G. Lee, S. Kim, S. Kim, Y. S. Lee, *Adv. Electron. Mater.* **2021**, *7*, 2100185.
[27] H. Kwak, C. Lee, C. Lee, K. Noh, S. Kim, *Semicond. Sci. Technol.* **2021**, *36*, 114002.
[28] J. Lee, R. D. Nikam, M. Kwak, H. Hwang, *ACS Appl. Mater. Interfaces* **2022**, *14*, 13450.
[29] Y. Li, E. J. Fuller, J. D. Sugar, S. Yoo, D. S. Ashby, C. H. Bennett, R. D. Horton, M. S. Bartsch, M. J. Marinella, W. D. Lu, A. A. Talin, *Adv. Mater.* **2020**, *32*, 2003984.
[30] R. D. Nikam, M. Kwak, H. Hwang, *Adv. Electron. Mater.* **2021**, *7*, 2100142.
[31] H. Lee, D. G. Ryu, G. Lee, M.-K. Song, H. Moon, J. Lee, J. Ryu, J.i-H. Kang, J. Suh, S. Kim, J. Lim, D. Jeon, S. Kim, J. Kim, Y. S. Lee, *Adv. Electron. Mater.* **2022**, *8*, 2200378.

[32] N. Kim, H. Kang, H. W. Kim, E. Hong, J. Woo, *Appl. Phys. Lett.* **2022**, *121*, 072105.
[33] G. Gregori, M. Shirpour, J. Maier, *Adv. Funct. Mater.* **2013**, *23*, 5861.
[34] S. T. Keene, A. Melianas, Y. Van De Burgt, A. Salleo, *Adv. Electron. Mater.* **2019**, *5*, 1800686.
[35] D. S. Kim, V. J. Watkins, L. A. Cline, J. Li, K. Sun, J. D. Sugar, E. J. Fuller, A. A. Talin, Y. Li, *Adv. Electron. Mater.* **2023**, *9*, 2200958.
[36] G. Vázquez, I. González, *Electrochim. Acta* **2007**, *52*, 6771.
[37] X. Chen, W. Li, L. Wang, Y. Zhao, X. Zhang, Y. Li, J. Zhao, *Mater. Chem. Phys.* **2021**, *270*, 124745.
[38] J. Zhang, S. Ricote, P. V. Hendriksen, Y. Chen, *Adv. Funct. Mater.* **2022**, *32*, 2111205.
[39] Y. Yan, J. B. Grinderslev, T. Burankova, S. Wei, J. P. Embs, J. Skibsted, T. R. Jensen, *J. Phys. Chem. Lett.* **2022**, *13*, 2211.
[40] S. Ikegawa, F. B. Mancoff, J. Janesky, S. Aggarwal, *IEEE Trans. Electron Devices* **2020**, *67*, 1407.
[41] R. Dominko, J. Bitenc, R. Berthelot, M. Gauthier, G. Pagot, V. Di Noto, *J. Power Sources* **2020**, *478*, 229027.
[42] P. Canepa, G. Sai Gautam, D. C. Hannah, R. Malik, M. Liu, K. G. Gallagher, K. A. Persson, G. Ceder, *Chem. Rev.* **2017**, *117*, 4287.
[43] R. Wang, C.-C. Chung, Y. Liu, J. L. Jones, V. Augustyn, *Langmuir* **2017**, *33*, 9314.
[44] R. Wang, S. Boyd, P. V. Bonnesen, V. Augustyn, *J. Power Sources* **2020**, *477*, 229015.
[45] S. Lee, J. Moon, H. M. Bintang, S. Shin, H.-G. Jung, S.-H. Yu, S. H. Oh, D. Whang, H.-D. Lim, *J. Mater. Chem. A* **2021**, *9*, 10838.
[46] Z. Liang, C. Ban, *Angew. Chem.* **2021**, *60*, 11036.
[47] O. F. Schirmer, E. Salje, *Solid State Commun.* **1980**, *33*, 333.
[48] E. Bousquet, H. Hamdi, P. Aguado-Puente, E. K. H. Salje, E. Artacho, P. Ghosez, *Phys. Rev. Research* **2020**, *2*, 012052.
[49] N. Bondarenko, O. Eriksson, N. V. Skorodumova, *Phys. Rev. B* **2015**, *92*, 165119.
[50] P. M. Woodward, A. W. Sleight, T. Vogt, *J. Phys. Chem. Solids* **1995**, *56*, 1305.
[51] S. Kim, T. Todorov, M. Onen, T. Gokmen, D. Bishop, P. Solomon, K.-T. Lee, M. Copel, D. B. Farmer, J. A. Ott, T. Ando, H. Miyazoe, V. Narayanan, J. Rozen, in *2019 IEEE International Electron Devices Meeting (IEDM)*, **2019**, pp. 35.7.1–35.7.4.
[52] Q. Zhong, J. R. Dahn, K. Colbow, *Phys. Rev. B* **1992**, *46*, 2554.
[53] L. Flermans, J. Vennik, *J. Electron Spectrosc. Relat. Phenom.* **1977**, *11*, 171.
[54] O. Bouvard, A. Krammer, A. Schüler, *Surf. Interface Anal.* **2016**, *48*, 660.
[55] T. H. Fleisch, G. J. Mains, *J. Chem Phys* **1982**, *76*, 780.
[56] V. Lokhande, A. Lokhande, G. Namkoong, J. H. Kim, T. Ji, *Results Phys* **2019**, *12*, 2012.
[57] D. Grier, G. McCarthy, ICDD grant-in-aid, Fargo, North Dakota, USA, **1991**.
[58] C. H. Rüscher, K. R. Dey, T. Debnath, I. Horn, R. Glaum, A. Hussain, *J. Solid State Chem.* **2008**, *181*, 90.
[59] N. Fairley, V. Fernandez, M. Richard-Plouet, C. Guillot-Deudon, J. Walton, E. Smith, D. Flahaut, M. Greiner, M. Biesinger, S. Tougaard, D. Morgan, J. Baltrusaitis, *Appl. Surf. Sci. Adv.* **2021**, *5*, 100112.
[60] P. E. Blöchl, *Phys. Rev. B* **1994**, *50*, 17953.
[61] G. Kresse, J. Hafner, *Phys. Rev. B* **1993**, *47*, 558.
[62] G. Kresse, J. Hafner, *Phys. Rev. B* **1994**, *49*, 14251.
[63] G. Kresse, J. Furthmüller, *Phys. Rev. B* **1996**, *54*, 11169.
[64] G. Kresse, J. Furthmüller, *Comput. Mater. Sci.* **1996**, *6*, 15.
[65] G. Kresse, D. Joubert, *Phys. Rev. B* **1999**, *59*, 1758.
[66] J. Sun, A. Ruzsinszky, J. P. Perdew, *Phys. Rev. Lett.* **2015**, *115*, 036402.
[67] S. L. Dudarev, G. A. Botton, S. Y. Savrasov, C. J. Humphreys, A. P. Sutton, *Phys. Rev. B* **1998**, *57*, 1505.
[68] M. Youssef, B. Yildiz, *Phys. Rev. B* **2012**, *86*, 144109.